ACS Catalysis

pubs.acs.org/acscatalysis
Research Article

Hydrogenation of Mixed Ir−Ti Oxide: A Powerful Concept to Promote the Oxygen Evolution Reaction in Acidic Water Electrolysis

Wei Wang, Matej Zlatar, Yu Wang, Phillip Timmer, Alexander Spriewald-Luciano, Lorena Glatthaar, Serhiy Cherevko, and Herbert Over*

Cite This: ACS Catal. 2025, 15, 6721−6730
Read Online

ABSTRACT: A simple and versatile strategy of catalytic promotion is presented that is able to significantly improve both the catalytic propane combustion and most notably the oxygen evolution reaction activity in acidic water electrolysis of phase-pure $Ir_{0.3}Ti_{0.7}O_2$ by hydrogen incorporation of 26 at% into $Ir_{0.3}Ti_{0.7}O_2$ through H_2 exposure at 150 °C without compromising the *long-term* stability. The most attractive feature of hydrogen promotion is the prospect of improving oxidation catalysis for an entire class of materials, namely, mixed oxides, and for various oxidation reactions, regardless of whether they belong to thermal or electrocatalysis. Hydrogen promotion is proposed to be routinely tested in materials screening of mixed oxides in oxidation catalysts.

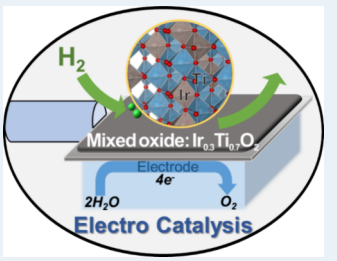

KEYWORDS: *solid solution of oxides, hydrogen incorporation, promotor, oxygen evolution reaction, acidic water electrolysis*

1. INTRODUCTION

Proton exchange membrane water electrolysis (PEM-WE) is currently the most effective way to produce green hydrogen from intermittent renewable energy sources that can serve both as a critical commodity chemical and an attractive energy storage medium.[1,2] The counterreaction to the hydrogen evolution (HER) is the oxygen evolution reaction (OER), which takes place at the anode under acidic conditions and high anodic potential so that currently only iridium-based oxides can withstand this harsh environment in the long term and are also therefore used in commercial PEM-WE.[3,4] However, iridium is one of the scarcest elements in the Earth's crust, so that reducing the Ir load while maintaining the overall activity in the OER would be highly desirable. Two strategies are conceivable: one is to increase the number of active sites per Ir mass, and the other is to increase the intrinsic activity of Ir-based active sites.[5−7]

Lower Ir loadings has been achieved, for example, by diluting IrO_2 with stable rutile TiO_2 in the form of a solid solution.[8,9] From dimensionally stable anode (DSA) technology, it is known that 30 mol % Ir is sufficient to maintain a high electronic conductivity of the coating (Ir_30:30 mol % IrO_2 and 70 mol % rutile TiO_2),[10,11] albeit the overall activity is expected to decrease with the number of active sites. Another strategy to reduce the iridium loading is to use porous materials with high surface-to-bulk ratios and good accessibility to the active site[12] or to coat a more abundant transition metal core with an ultrathin IrO_2 shell.[13] The formation of 2D Ir metallene oxides allows most of the Ir atoms (which are now all on the surface and accessible) to be utilized in the catalytic OER.[14]

There are a number of ways in which the intrinsic activity of IrO_2 can be improved.[15] The simplest strategy is to use Ir metal, which is more active than IrO_2, but unfortunately, metallic Ir is also much less stable than IrO_2.[16,17] Alternatively, one can reduce the crystallinity of IrO_2 (amorphous IrO_2), which encompasses IrO_2 with a higher concentration of unsaturated and therefore active sites.[18−21] Lattice water-assisted short-range ordered iridium oxide ($IrOx{\cdot}nH_2O$)[22] has been shown to be an efficient OER electrocatalyst for highly stable acidic water oxidation. Doping engineering is another option to improve the intrinsic activity of IrO_2,[23,24] as demonstrated, for example, with mixed $Ru_{1-x}Ir_xO_2$.[25−27]

Recently, we have introduced the concept of incorporated hydrogen[28] as an efficient promoter in oxidation catalysis. It was shown that 18 atom % hydrogen can be incorporated into the mixed oxide $Ru_{0.3}Ti_{0.7}O_2$ by hydrogen exposure at 250 °C, leading to a significant improvement in the catalytic activity of the total oxidation reaction of propane and of the HCl oxidation to recover Cl_2. It was suggested that this promoting effect of hydrogen incorporation may not be limited to thermal oxidation catalysis but could be fully exploited in electrocatalysis such as the demanding OER.[28]

In order to reveal clear structure−activity correlations, phase-pure mixed oxide Ir_30_pp is prepared, and the promoting effect of inserted hydrogen is tested in two

Received: January 22, 2025
Revised: March 15, 2025
Accepted: April 2, 2025
Published: April 10, 2025

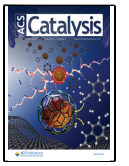

https://doi.org/10.1021/acscatal.5c00588
ACS Catal. 2025, 15, 6721−6730

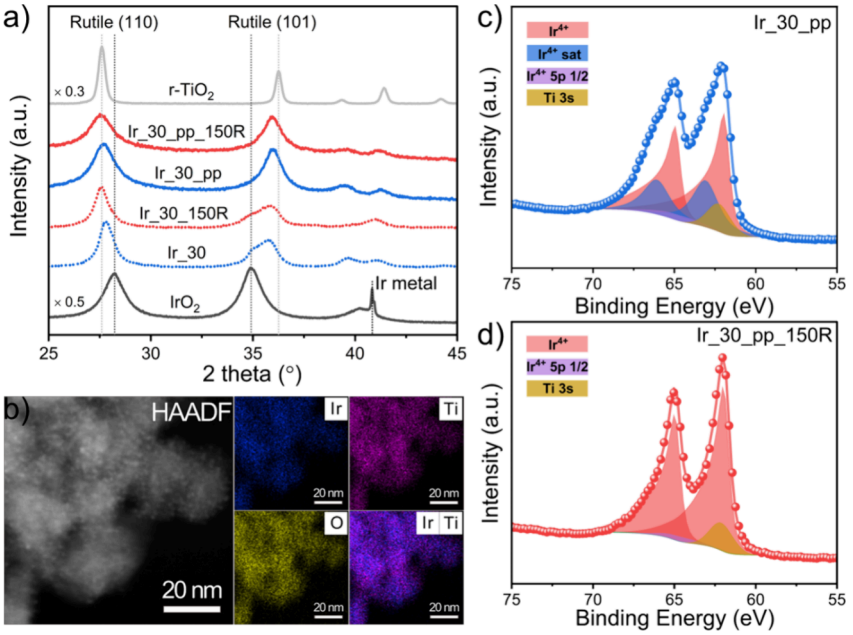

Figure 1. (a) Powder XRD of Ir_30 and phase pure Ir_30_pp before and after mild reduction at 150 °C for 3 h in 4% H_2 (Ir_30_150R, Ir_30_pp_150R). (b) HAADF and element mapping of Ir_30_pp_150R. Ir 4f XPS spectra of phase-pure (c) Ir_30_pp and (d) Ir_30_pp_150R after mild hydrogenation at 150 °C. The deconvolution of the spectra in various species (Ir^{4+}, Ir^{4+}-satellite, Ir^{4+}5p, Ti 3s) are indicated, while the specific fitting parameters are compiled in Table S3.

prototypical oxidation reactions, one taken from thermal catalysis and the other from electrocatalysis. In addition to the catalytic combustion of propane, which is an important reaction for the after-treatment of exhaust gas of liquid petroleum gas-powered engines,[29] we demonstrate the promoting effect of inserted hydrogen for the acidic oxygen evolution reaction (OER).

2. MATERIALS AND METHODS

Preparation of Ir_30: First, the mixed Ir−Ti oxide (with 30 mol % Ir) is prepared via a conventional sol−gel method as previously reported:[28] 20 mmol anhydrous citric acid (Sigma-Aldrich 99.5%) and 0.6 mmol $IrCl_4 \cdot H_2O$ (fluorochem, 99.9%) are dissolved into 40 mL deionized water. Then, 5 mL of anhydrous ethanol containing 1.4 mmol of titanium butoxide (Sigma-Aldrich, 97%) is added dropwise to the solution. After sufficient stirring, the pH of the mixture is adjusted to ∼6 before heating to 90 °C for evaporation. The resulting gel is dried overnight and calcined at 400 °C for 4 h with a heating rate of 2 °C/min. The final sample is designated as Ir_30.

Preparation of Ir_30_pp: As shown in XRD (Figure 1a), Ir_30 is not phase pure but consists of a mixture of pure IrO_2 and $Ir_xTi_{1-x}O_2$. In order to synthesize phase-pure Ir_30 (Ir_30_pp), which allows to study clear structure−function correlations in the OER, a modified polymer complex route based on the sol−gel method is applied:[30] 0.3 mmol $Ir(Acac)_3$ (Fluorochem, 99.9%) is dissolved in a mixture of 5 mL methanol and 5 mL acetylactone to form a homogeneous light yellow solution. 0.7 mmol of titanium(IV)-isopropoxide (Sigma-Aldrich. 99.5%) is injected under nitrogen protection into 9.8 mL of 0.2 M citric acid 1-proponal solution, and then 4.8 mL of acetylactone is added to stabilize the titanium precursor. After thorough mixing, 9.8 mL of ethylene glycol is added, and the resulting solution is further mixed with the above $Ir(Acac)_3$ solution. Finally, 8.1 mL of acetonitrile is added to the solution. After the mixture is stirred for 1 h, 1 mL of concentrated HNO_3 is added, and the final mixture is heated in an oil bath at 100 °C for 7 days. The resulting gel is calcined at 400 °C for 4 h in several heating steps (see Table S1). The final sample is referred to as Ir_30_pp.

Hydrogen incorporation: The Ir_30 or Ir_30_pp catalyst is placed in a quartz boat and hydrogenated for 3 h under 4%H_2/N_2 in a tubular furnace at 150 °C; the heating rate is 2 °C/min. The resulting catalysts are called Ir_30_pp_150R.

Characterization of catalysts: Powder X-ray diffraction (XRD) measurements are performed on a Panalytical Empyrean diffractometer, using a Cu Kα source operated at 40 kV and 40 mA. The XRD scan is performed in an angle range from 15 to 75°. The average crystallite size is evaluated using the Scherrer equation, while the composition of the catalyst is estimated by using Vegard's law. Scanning transmission electron microscopy (STEM) images of the catalyst are obtained using a ThermoFisher Talos F200X transmission electron microscope. High-angle annular dark field (HAADF) STEM images are taken using a convergence half angle of 25 mrad and inner and outer collection angles of 47 and 200 mrad, respectively. Energy dispersive X-ray spectroscopy (EDS) is performed using four in-column Super-X detectors. Scanning electron microscopy (SEM) images and EDS mapping are taken by a Gemini SEM 560 instrument. X-ray photoelectron spectroscopy (XPS) is performed with a PHI VersaProbe II spectrometer, using a photon energy of 1486.6 eV (monochromatized Al−Kα line). XPS spectra are analyzed using CasaXPS software (version 2.3.17). Thermogravimetric (TG) analysis is performed on a STA 409PC thermoscale (Netzsch) coupled to a QMG421 quadrupole mass spectrometer (MS, Balzers) with an ionization energy of 70 eV. Approximately 20 mg of Ir_30_pp and Ir_30_pp_150R catalysts is heated under synthetic air (30 sccm/min) from room temperature to 500 °C with a heating rate of 10 °C/min. Sample pretreatment and storage conditions are kept constant. Due to the low signal-to-

https://doi.org/10.1021/acscatal.5c00588
ACS Catal. 2025, 15, 6721−6730

noise ratio, we do not directly determine the hydrogen capacity by monitoring the H_2 in an inert atmosphere with MS. Instead, we performed a kind of temperature-programmed oxidation experiment, where the total amount of incorporated hydrogen was quantified by the amount of produced water in an oxidizing atmosphere during temperature ramping.

Catalytic Tests: (a) Total propane oxidation: The catalytic test for propane oxidation is performed in a home-built flow reactor system.[31] A homogeneous mixture of 20 mg of catalyst and 40 mg of quartz sand is placed in the center of a quartz tube to which a constant flow of the reactant gas (1 vol % C_3H_8, 5 vol % O_2, balanced with 94 vol % N_2) is continuously fed at a rate of 100 cm^3 STP min^{-1} (sccm). This corresponds to a weight hourly space velocity (WHSV) of 345000 $mL \cdot g^{-1} \cdot h^{-1}$. A nondispersive infrared (NDIR) sensor is used to measure the volumetric concentration of CO/CO_2 and C_3H_8. The catalyst is ramped from room temperature to 300 °C at a rate of 1 °C/min. The propane conversion is determined using the following equation:

$$X_{C_3H_8} = \frac{c(CO_2)}{c_{max}(CO_2)}$$

where $c(CO_2)$ is the concentration of CO_2 at the outlet of the reactor during the temperature ramp and $c_{max}(CO_2)$ is the full conversion state concentration of CO_2. The carbon mass balance is carefully checked and guaranteed for each sample. The space-time yield (STY, $mol_{(CO_2)} \cdot kg^{-1}_{(Cat)} \cdot h^{-1}$) is used as the activity descriptor.

(b) Oxygen evolution reaction (OER): The OER is performed in a three-electrode system using a NOVA electrochemical workstation at room temperature. A 0.05 M H_2SO_4 solution is used as the electrolyte, and Pt wires and Ag/AgCl electrode (KCl saturated) are the counter and reference electrodes, respectively. Before the measurement, the catalyst film is prepared as a working electrode. First, the catalyst ink is prepared by ultrasonicating a mixture of 4 mg of catalyst, 20 μL of 5% Nafion solution (Sigma-Aldrich), 0.25 mL of anhydrous ethanol, and 0.75 mL of ultrapure H_2O for 40 min. After forming a homogeneous solution, 5 μL of the catalyst ink is deposited onto a glassy carbon electrode with a 3 mm diameter (area: 0.07 cm^2) and then dried at room temperature. The catalyst loading per surface area is 280 $\mu g/cm^2$. A linear sweep voltammetry (LSV) program is used to quantify the activity of the anode: The electrode potential is varied from 1.0 to 1.6 V vs RHE (reversible hydrogen electrode) with a scan rate of 10 mV/s, and the current density is measured. For various electrode potentials, electrochemical impedance spectra are acquired to determine the conductivity of the catalyst coating and the charge transfer resistance.

To evaluate the stability of phase pure and hydrogenated iridium catalysts, real-time monitoring of iridium and titanium dissolution under varying electrochemical potentials within the OER range is achieved using a custom polycarbonate scanning flow cell (SFC), connected to an inductively coupled plasma mass spectrometer (ICP-MS, PerkinElmer NexION 350X).[32,33] To prepare working electrodes, catalyst powders are dispersed in a 7:1 ratio of ultrapure water to IPA, with the addition of a perfluorinated Nafion ionomer solution (Sigma-Aldrich, 5 wt %) as a binder. The resulting ink is ultrasonicated for 20 min (4 s on/2 s off pulses) using a probe sonicator (Branson Ultrasonics SFX150), followed by pH adjustment to approximately 11 using 1 M KOH. Finally, 2.3 μL aliquots of this ink are carefully dropped onto an Au foil backing electrode (25 × 25 mm, 99.95%, Alfa Aesar).[34] The surface area of these spots is then estimated using a Keyence VK-X250 profilometer, and the final catalyst loading is estimated to be 280 $\mu g\ cm^{-2}$. For the counter electrode, a glassy carbon rod (HTW, Sigradur G) is connected at the SFC inlet through a T-connector, while a Ag/AgCl reference electrode (Metrohm, Germany) is connected to the outlet through a capillary to prevent Cl^- contamination. The Au foil with the drop-casted catalysts is positioned on an XYZ translation stage (Physik Instrumente M-403) and connected with Cu tape. All experiments are conducted in a 0.05 M H_2SO_4 electrolyte solution, flowing at ~3.5 μL/s and prepared by diluting concentrated H_2SO_4 (Suprapure 96%, Merck) with ultrapure water to ensure minimal impurities (less than 2% w/w salts and organics). Electrochemical analyses are performed using a Biologic potentiostat (VSP-150, Biologic), and recorded potentials are presented on the reversible hydrogen electrode (RHE) scale. To maintain accuracy, the ICP-MS is calibrated daily using a three-point method with standard solutions (Merck Certipur, Ir, Ti 1000 mg L^{-1}) in the same electrolyte, supplemented with internal standards (^{187}Re for ^{193}Ir and ^{45}Sc for ^{47}Ti) with similar ionization energy and mass as measured analyte to compensate for any interferences, matrix effects, and instrumental variations.

The electron paramagnetic resonance (EPR) spectra are measured using a Bruker EMX PLUS spectrometer at 100 K, and 20 mg of the sample is used. The measurement parameters are as follows: a center field of 3320.00 G, a microwave frequency of 9.30 GHz, and power of 3.170 mW. The g factor is calculated via $g = h\nu/\beta H$, where h is the Planck constant, ν is the microwave frequency, β is the Bohr magneton, and H is the magnetic field.[35,36]

The ^{1}H solid-state NMR experiments are performed using standard methodologies with a Bruker Avanced NEO 400 M spectrometer at frequencies of 400.1 MHz (^{1}H). Freshly prepared samples (100 mg) are used to obtain a quantitative result. One-dimensional data sets are acquired on samples spun at 15 kHz using 2.0 mm magic-angle spinning (MAS) probes.[37]

3. RESULTS

As indicated by powder X-ray diffraction (XRD) in Figure 1a, the Ir−Ti oxide system faces a pronounced miscibility gap: Ir_30 consists of a mixed $Ir_xTi_{1-x}O_2$ and pure IrO_2 (both in a rutile structure). Upon hydrogenation at 150 °C (Ir_30_150R), part of the IrO_2 is reduced to metallic Ir in face-centered cubic (fcc) structure and the rutile $Ir_xTi_{1-x}O_2$ diffraction peaks shift slightly, which can be interpreted as due to hydrogen incorporation, similar to the case of Ru_30 hydrogenation.[28] Since the strongest Ir metal diffraction peak at 41° overlaps with the IrO_2 diffraction features (cf. Ir_100 scan in Figure 1a), the formation of Ir metal can only be inferred from the observed intensity variation in the double peak around 39−41° of Ir_30 and Ir_30_150R. Deconvolution of rutile-related XRD peaks in Figure S1 shows that the intensity of IrO_2-related diffraction peaks is indeed significantly reduced, thus supporting the transformation of IrO_2 to Ir metal upon 150R treatment. X-ray photoelectron spectroscopy (XPS) of Ir_30 (Ir 4f in Figure S2) shows that Ir is exclusively in the 4+ oxidation state, and no metallic Ir feature is detected,

https://doi.org/10.1021/acscatal.5c00588
ACS Catal. 2025, 15, 6721−6730

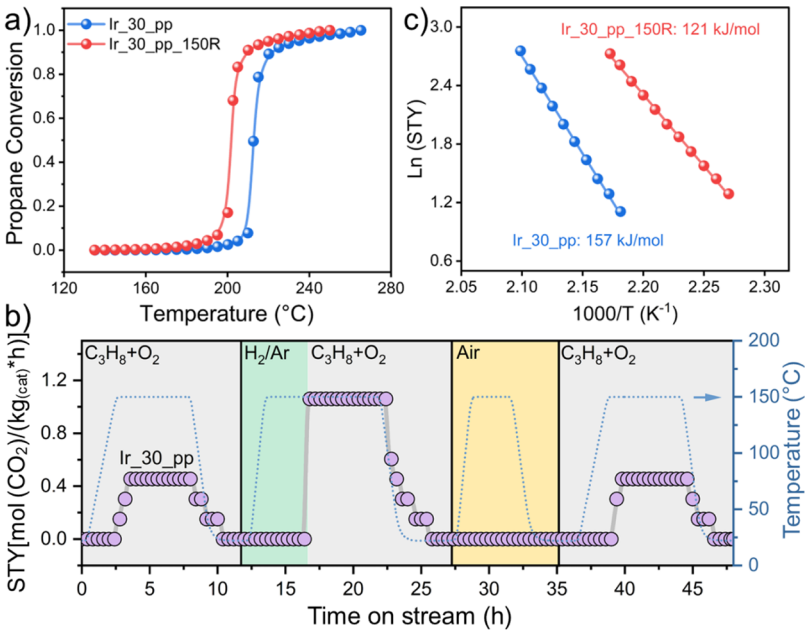

Figure 2. Activity data of phase pure Ir_30_pp and Ir_30_pp_150R in the total oxidation of propane: 1 vol % C_3H_8, 5 vol % O_2 balanced by N_2; total volume flow rate: 100 sccm/min; temperature ramp: 1 K/min. (a) Conversion curves and (b) space−time yield (STY in mol product per kg catalyst and time) of Ir_30_pp in the catalytic propane combustion as a function of the reaction time when cycling the reaction temperature between 30 and 150 °C in the same reaction mixture as in (a) (gray background). Hydrogenation of Ir_30_pp occurs during temperature ramping (1 K/min) from 30 to 150 °C in 4% H_2/Ar with total volume flow of 50 sccm/min (green background). When reaching 150 °C, the gas composition is switched to the reaction mixture (gray background), revealing a substantial increase in activity. After cooling to 30 °C the atmosphere is switched back to air (yellow background) and the temperature is cycled between 150 and 30 °C after which the activity is identical to that of the as-prepared Ir_30_pp. (c) Arrhenius plots of Ir_30_pp and Ir_30_pp_150R (for conversion lower than 5%).

while a strong spectral signature of metallic Ir appears in the Ir 4f XP spectrum of Ir_30_150R.

For the interpretation of hydrogen-induced activity enhancement in the OER, the miscibility gap of Ir_30 poses a problem since Ir is a much better OER catalyst than IrO_2. Therefore, possible activity enhancements in the OER of Ir_30 cannot be unambiguously attributed to hydrogen incorporation into mixed $Ir_{0.3}Ti_{0.7}O_2$. For this reason, we prepare phase-pure Ir_30 (Ir_30_pp) by a sophisticated Pechini approach adapted from the literature.[30] The phase purity of Ir_30_pp and Ir_30_pp_150R is confirmed by XRD in Figure 1a. In the diffraction pattern, only diffraction features of rutile mixed $Ir_xTi_{1-x}O_2$ appear, which are characteristically shifted with respect to those of pure IrO_2 and r-TiO_2. The derived lattice parameters (summarized in Table S2) can be used to estimate the average composition based on Vegard's rule: According to Figure S3, the Ir concentration is about 30 mol %, which is close to the nominal composition of Ir_30_pp. When Ir_30_pp is mildly hydrogenated at 150 °C (Ir_30_pp_150R), the diffraction peaks of mixed $Ir_xTi_{1-x}O_2$ are slightly shifted with respect to those of Ir_30_pp, while no metallic Ir features appear in the diffraction pattern. This behavior suggests that hydrogen is incorporated into the mixed oxide lattice without forming a metallic phase of Ir. The composition of Ir_30_pp and Ir_30_pp_150R is independently determined by energy dispersive X-ray spectroscopy (EDS) (cf. Figure S4) and turns out to be 28−29 mol % Ir (cf. Table S2). Using high-angle annular dark field (HAADF) and elemental mapping (see Figure 1b), it is evident that Ti, Ir, and O are uniformly distributed in Ir_30_pp_150R. No enrichment of Ir, in the form of either IrO_2 or metallic Ir, is evident from the elemental mapping of Ir.

In the XPS experiments summarized in Figure 1c,d and deconvoluted by various species (Ir^{4+}, Ir^{4+}-satellite, Ir^{4+}5p, Ti 3s) no metallic Ir feature is observed in the Ir 4f spectra of Ir_30pp and Ir_30_pp_150R, proving that Ir_30_pp_150R, and thus Ir_30_pp is phase pure in the near-surface region regardless of crystallinity; the specific fitting parameters are compiled in Table S3, which are consistent with corresponding literature values.[38] The pronounced asymmetry of Ir^{4+} components is caused by electron−hole pair excitation of the metallic conducting oxide of Ir_30_pp and Ir_30_pp_150R.[39,40] Hydrogenation of Ir_30_pp at 150 °C does not change the oxidation state of Ir, which remains in the 4+ oxidation state. However, the shakeup satellite features disappear in the Ir 4f XP spectrum.

Figure S5 shows the Ir 4f difference spectrum of Ir_30_pp_150R and Ir_30_pp, from which clearly only a double feature remains, which is attributed to the shakeup satellite features of Ir^{4+}.[39,40] Mild reoxidation of Ir_30_pp_150R at 300 °C (Ir_30_pp_150R_300O) causes the satellite feature to reappear (Figure S6). In Figure S6b, the difference spectrum of Ir_30_150R_300O and Ir_30_pp is identical to the noise level, confirming the reversible behavior upon mild hydrogenation and oxidation. In XRD, the rutile diffraction features of Ir_30_pp_150R_300O are shifted back to the position of Ir_30_pp (cf. Figure S7a), thus demonstrating a fully reversible behavior of hydrogen insertion and removal upon mild hydrogenation and subsequent mild reoxidation.

The slight shift in the diffraction features of Ir_30_pp upon hydrogenation at 150 °C (cf., Figure 1a) might suggest only a small amount of hydrogen incorporation. However, this is not the case. Thermogravimetric (TG) analysis coupled to a mass

https://doi.org/10.1021/acscatal.5c00588
ACS Catal. 2025, 15, 6721−6730

spectrometer (MS in Figure S8a and the corresponding TGA signal in Figure S8b) quantifies that 26 at% hydrogen is incorporated into Ir_30_pp_150R, which is about the same molar percentage as that of Ir in Ir_30_pp.

Recently, the promoting effect of hydrogen incorporation in mixed oxides of 30 mol % of RuO_2 and 70 mol % rutile TiO_2 (Ru_30) has been reported for two catalytic oxidation reactions,[28] namely, the propane combustion and the HCl oxidation. Therefore, we also expect a promoting effect of the incorporated hydrogen in Ir_30_pp for the total oxidation of propane; the corresponding conversion curves are summarized in Figure 2a. Ir_30_pp reaches 90% conversion at 215 °C, while after hydrogenation at 150 °C (Ir_30_pp_150R) 90% of the propane is already converted at 205 °C.

The apparent activation energies of Ir_30_pp and Ir_30_pp_150R are 157 and 121 kJ/mol, respectively (see Figure 2c). Since neither the XRD nor the O 1s, Ti 2p, and Ir 4f XP spectra change when Ir_30_pp is hydrogenated at low temperature (except for suppression of the satellite feature that is assumed to be a bulk property[39]), we presume that the number of active sites of Ir_30_pp and Ir_30_pp_150R is preserved. The observed variation in apparent activation energy upon hydrogenation is pronounced and may therefore indicate that the interaction of the reaction intermediates with the catalyst is affected in the rate controlling step.

Hydrogenation of Ir_30_pp can also be performed in situ in the flow reactor, as summarized in Figure 2b. When Ir_30_pp is exposed to a hydrogen atmosphere during temperature ramping from room temperature to 150 °C, the catalytic propane combustion activity of hydrogenated Ir_30_pp at 150 °C is significantly increased from 0.5 for Ir_30_pp to 1.1 $mol(CO_2)\ kg^{-1}(Cat)\ h^{-1}$. Temperature ramping of Ir_30_pp_150R in air leads to the same activity as for the as-prepared Ir_30_pp, indicating a reversible activity behavior of Ir_30_pp in catalytic propane combustion upon hydrogenation and mild reoxidation (Figure S7b).

We now demonstrate the promoting effect of the incorporated hydrogen in Ir_30_pp for the OER under acidic conditions by comparing the mass-normalized current−voltage curves (linear sweep voltammograms, LSV) of phase pure Ir_30_pp and Ir_30_pp_150R in the OER potential range (Figure 3a). It can be seen that Ir_30_pp is similarly active to Ir_100 (pure IrO_2, used here as a reference) in the OER, while the mass-normalized current of Ir_30_pp_150R is significantly higher than that of Ir_100. At an electrode potential of 1.6 V (vs RHE), the mass-normalized current summarized in Figure 3a is approximately seven times higher, meaning that seven times less Ir is required in Ir_30_150R to achieve the same catalytic performance as the pure IrO_2 reference catalyst. The corresponding current densities as a function of the electrode potential are shown in the inset of Figure 3a. The promoting effect of Ir_30_pp_150R is reflected by an overpotential gain of about 60−70 mV at a current density of 1 mA/cm^2.

The Tafel plots are collected in Figure S9 for Ir_30_pp and Ir_30_pp_150R and compared to those of pure Ir_100. From these plots, the Tafel slope, a characteristic parameter describing the reactivity of an electrocatalyst[41,42] can be determined to be 73 mV/dec (Ir_30_pp), 57 mV/dec (Ir_30_pp_150R), and 48 mV/dec (Ir_100). Within the generalized Butler−Volmer formalism, these differences in Tafel slopes indicate a variation in the intrinsic activity.[43] Comparison with the literature: The found value for Ir_100 is consistent with the reported Tafel slopes of pure single crystalline IrO_2(110) (49 mV/dec^3)[44] and polycrystalline IrO_2 (39−48 mV/dec).[45]

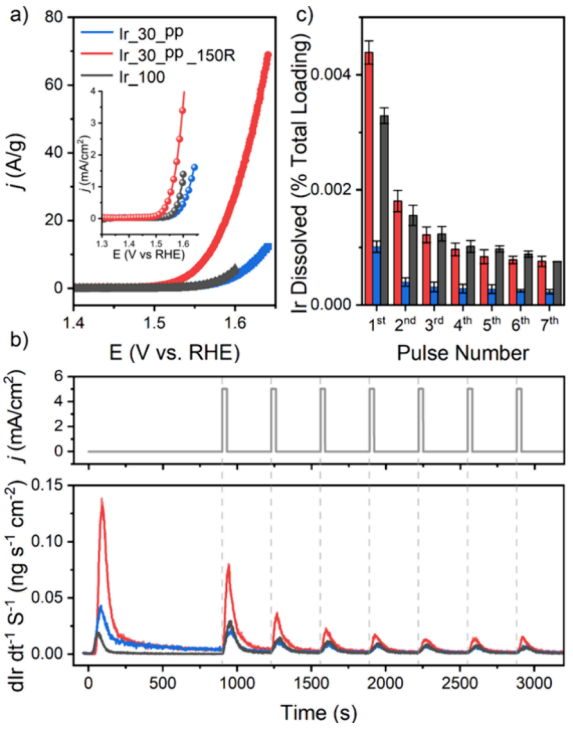

Figure 3. (a) Catalytic oxidation activity (given in current per gram of active component IrO_2) of phase pure Ir_30_pp and Ir_30_pp_150R (in comparison with Ir_100) in the oxygen evolution reaction (OER), the anodic reaction of the water electrolysis. The corresponding current densities as a function of the electrode potential are shown in the inset. (b) Stability experiments: summary of the SFC-ICP-MS experiments of Ir_30_pp, Ir_30_pp_150R, and commercial IrO_2. Electrochemical protocol of consecutive galvanostatic holds (OER pulses) monitored Ir dissolution rate at the ICP-MS. (c) Total amount of Ir dissolution depending on the OER pulse number.

It has been shown for some OER catalysts that increased activity is associated with decreased stability.[46] Therefore, the dissolution rates of Ir from Ir_30_pp and Ir_30_pp_150R are quantified using a scanning flow cell (SFC) connected to an inductively coupled plasma mass spectrometer (ICP-MS) under identical OER conditions.[33] The electrochemical protocol (see Figure 3b) starts with bringing the electrode surface into contact with the SFC followed by 6 min at the open circuit potential (OCP). Then, seven consecutive galvanostatic holds (OER pulses) are applied at 5 $mA{\cdot}cm^{-2}$ for 30 s each, separated by 4 min at an OCP each. A trend of stabilization, i.e., a decrease in the total amount of Ir dissolution with an increasing number of consecutive OER pulses, is clearly visible for both electrodes. For the Ir_30_pp model electrode, Ir dissolution decreases from 1.3 ± 0.2 $ng{\cdot}cm^{-2}$ after the first OER pulse to 0.35 ± 0.02 $ng{\cdot}cm^{-2}$ after the seventh pulse, while in the case of the Ir_30_pp_150R electrode the decrease goes from 5.0 ± 0.1 $ng{\cdot}cm^{-2}$ to 0.95 ± 0.02 $ng{\cdot}cm^{-2}$ (cf. Figure 3b,c). Finally, steady state conditions are reached in the dissolution. The stability of Ir_30_pp is very high (as expected) and is slightly higher than that of commercial IrO_2 (cf. Figure 3c).[47] For Ir_30_pp_150R the dissolution rate of Ir increases by a factor of 3, indicating that the anodic dissolution stability does not deteriorate significantly and is virtually identical with that of pure IrO_2. The

https://doi.org/10.1021/acscatal.5c00588
ACS Catal. 2025, 15, 6721−6730

stability is corroborated by the invariance of repeated LSV of Ir_30_pp_150R in the OER range (Figure S10). The concomitant dissolution rate of Ti is low and not affected by the hydrogenation (cf. Figure S11).

4. DISCUSSION

Hydrogenation of mixed oxides at mild temperatures is a rather general concept for hydrogen insertion into mixed oxides when appropriate combinations of parent oxides are chosen, i.e., one oxide is capable of activating H_2 dissociation, while the other oxide component stabilizes the mixed oxides against total reduction. The resulting synergy effect allows the mixed oxide to accumulate absorbed H in the bulk of the mixed oxide while maintaining structural integrity. This concept has been demonstrated with the mixed oxide of RuO_2 and TiO_2 and applied to thermal catalysis.[28,48] Here, this strategy is applied to another mixed oxide, namely the solid solution of IrO_2 and TiO_2 with 30 mol % IrO_2. Using a sophisticated Pechini synthesis route,[30] phase-pure Ir_30_pp consisting only of the $Ir_{0.3}Ti_{0.7}O_2$ phase can be produced. This allows us to draw firm conclusions about the active phase of Ir_30_pp in the acidic OER.

It is evident from this study that hydrogen incorporation promotes the oxidation catalysis (propane combustion and OER) of phase pure Ir_30_pp. However, the reason for the promoting effect is less clear since hydrogen incorporation modifies both the electronic structure and the geometric structure through lattice strain (shift and width of XRD peaks). The strain-induced activity enhancement was predicted by Mavrikakis et al.[49] within the so-called d-band model.[49−51] Therefore, "strain engineering" has been widely applied as a promising strategy in electrocatalysis for activity enhancement, especially for water electrolysis.[52−55] Differently strained IrO_2 films have been shown to correlate with activity variations in the OER.[56] However, in the case of Ir_30_pp, hydrogen incorporation induces only marginal strain into the mixed oxide lattice (cf. Figure 1a), which also explains the observed high stability of Ir_30_pp_150R under OER conditions.[57] Therefore, the effect of hydrogen promotion on the OER activity is most likely due to electronic modification by H insertion.

The change in the oxidation states of cations and anions in the mixed oxide due to hydrogen insertion can be deduced from the XPS experiments: Ti is always in Ti^{4+}, no additional OH feature is observed in O 1s, and the Ir species in Ir_30_pp_150R are always in the 4+ oxidation state. This is most evident from the difference spectra of Ti 2p and O 1s before and after hydrogenation (cf. Figure S12). Therefore, the incorporated hydrogen may be a hydride species $H^{-\delta}$ as discussed for hydrogenated Ru_30_250R.[28] Hydride formation has already been reported for hydrogenated CeO_2[58,59] and has been attributed to its remarkable catalytic performance in the partial hydrogenation of alkynes to alkenes.[60,61] However, in ^{1}H solid-state NMR experiments (cf. Figure S13) only protonic $H^{+\delta}$ species are observed, implying that H interacts with lattice O,[62−65] and the formation of a hydride species $H^{-\delta}$ can safely be ruled out for Ir_30_pp_150R. The incorporated hydrogen partly transfers the electron to the oxide without changing, however, the oxidation states of Ir, Ti, and O. All this experimental evidence points to an interstitial H species without forming pronounced O−H and Ir−H bonds (cf. Figure 4). There is also no evidence of lattice water, neither in the O 1s XP spectra nor in ^{1}H NMR, which could explain the improved OER activity due to lattice water.[22]

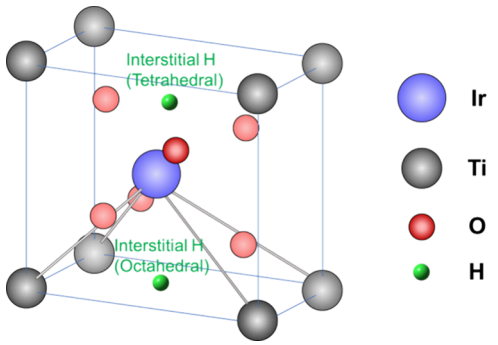

Figure 4. Structure model for hydrogenated $Ir_{0.3}Ti_{0.7}O_2$ solid solution and possible positions of incorporated hydrogen.

The catalytic combustion of hydrocarbons is fairly well understood. Important steps in the reaction mechanism include the first dehydrogenation step and the subsequent C−C decomposition.[66,67] With temperature-programmed reaction experiments iridium has been shown to be efficient in the activation of C−H and C−C bonds.[68] During the first propane dissociation step, the hydrogen is transferred to undercoordinated surface O and the propyl fragment adsorbs on an undercoordinated surface Ir site of Ir_30_pp. For the OER over oxide surfaces, the activity displays a volcano-like curve as a function of the free reaction energy of deprotonation reaction $OH \rightarrow O + H^+ + e^-$, which serves as the descriptor for the volcano curves.[69−71]

This universal behavior may be the missing link between the catalytic propane oxidation and the OER. Assuming that the first C−H activation step of propane is rate-determining in propane combustion, then hydrogenation of Ir_30_pp affects the activity of both catalytic reactions by modulating the O−H bond strength of the reaction intermediate. In our special case, we presume that hydrogenation of Ir_30_pp will weaken the Ir−O bonding and therefore increase the O−H bond strength, which facilitates both types of catalytic oxidation reactions by stabilizing the O−H reaction intermediate. This conclusion is supported by the variation of the apparent activation energy for the catalytic propane combustion while preserving the number of active sites.

Upon hydrogenation, the satellite peak disappears, and the removal of incorporated hydrogen by mild reoxidation causes the satellite to reappear. The reversible behavior of the satellite feature parallels the reversible hydrogen incorporation/removal that in turn modulates the oxidation activity both in the catalytic propane combustion and in the OER. However, the link between the suppression of the shape-up satellite and the improved catalytic activity in the propane combustion and the OER is not obvious. The shakeup satellite is due to a final state effect: Upon leaving the sample, the Ir 4f photoelectron of Ir^{4+} suffers an additional energy loss due to the excitation of electrons close to the Fermi level to a sharp unoccupied state in the d-projected partial density of states at 1 eV above the E_F of the ionized Ir atom.[39] Obviously, mild hydrogenation of Ir_30_pp suppresses this unoccupied state of the ionized Ir atom. From this finding, we can conclude that hydrogen incorporation does modify the electronic structure of Ir of Ir_30_pp_150R and therefore of the ionized Ir. Hydrogen

https://doi.org/10.1021/acscatal.5c00588
ACS Catal. 2025, 15, 6721−6730

may transfer electron density to this unoccupied state, thus suppressing the shakeup satellite. How the O−H bond strength is associated with the shakeup satellite is unknown and awaits future first-principles studies. However, the disappearance of the shakeup satellite upon H incorporation can serve as a benchmark experiment for future first-principles calculations in that proper theoretical modeling of the catalytic promotion effect of propane combustion and the OER by hydrogen incorporation in Ir_30_pp needs to result in a suppression of the shakeup satellite.

The high stability of Ir_30_pp_150R corroborates an oxidation state Ir of 4+ since the formation of Ir^{3+} should have led to higher Ir dissolution rates[72] than those observed in the present stability study (cf. Figure 3). Oxygen vacancies[73] in Ir_30_pp_150R are not formed by mild hydrogenation, as shown by EPR experiments (cf. Figure S14). Only high-temperature reduction at 600 °C produces vacancies of O in the mixed oxide. Recently, the formation of an electron-deficient O species has been reported[74] to be important for the high activity of amorphous IrO_2. However, there is no evidence of O^{1-} in EPR when one compares the EPR spectra of Ir_30_pp with those of Ir_30_pp_150R.

5. CONCLUSIONS

In conclusion, a novel and simple strategy is presented to enhance the catalytic oxidation activity of mixed oxides by hydrogen incorporation, exemplified by phase-pure $Ir_{0.3}Ti_{0.7}O_2$ (Ir_30_pp) and mild hydrogenation at 150 °C in 4 vol % H_2 for 3 h (Ir_30_pp_150R). The proper combination of parent oxides is critical, as one oxide should be able to activate H_2 dissociation (IrO_2) while the other oxide component (TiO_2) maintains structural integrity. Phase-pure $Ir_{0.3}Ti_{0.7}O_2$ can accommodate 26 at. % incorporated hydrogen in the oxide lattice, which has been shown to promote catalytic oxidation reactions from both thermal catalysis (propane combustion) and electrocatalysis (oxygen evolution reaction: OER) while only slightly compromising anodic stability against anodic dissolution. The promotion effect of hydrogen incorporation may be attributed to a weakening of the Ir−O bonding of bulk Ir_30_pp that in turn strengthens the O−H bonding at the surface, and therefore, the reaction intermediate (O−H) of the rate-limiting reaction steps in propane combustion and in the oxygen evolution reaction (OER). Further first-principles calculations are called for to settle this point. We propose that formixed oxide catalysts, hydrogen promotion should be routinely tested in materials screening of oxidation catalyts.

■ ASSOCIATED CONTENT

Supporting Information

The Supporting Information is available free of charge: The Supporting Information is available free of charge at https://pubs.acs.org/doi/10.1021/acscatal.5c00588.

Table of calcination program for the preparation of phase-pure Ir_30_pp; deconvolution of XRD pattern of Ir_30 and Ir_30_150R; decomposition of Ir 4f XP spectra of nonphase-pure Ir_30 and Ir_30 _150R; table of lattice parameter, grain size, and composition; Vegard plot to estimate the composition of Ir_30 and Ir_30_pp; SEM-EDS micrographs of Ir_30_pp; fitting parameters of XP spectra; Ir 4f difference spectrum of Ir_30_pp_150R and Ir_30_pp; Ir 4f difference spectrum of Ir_30_pp_150R and Ir_30_pp_150R_300O; XRD of Ir_30_pp_150R_300O and propane conversion curves; TG-MS experiments of Ir_30_pp and Ir_30_pp_150R; repeated LSV of Ir_30_pp_150R; Tafel plots of Ir_30_pp and Ir_30_pp_150R; Ti dissolution of Ir_30_pp and Ir_30_pp_150R; Ti 2p and O 1s spectra of Ir_30_pp and Ir_30_pp_150R; ^1H solid-state NMR spectra of Ir_30_pp and Ir_30_pp_150R; and EPR spectra of Ir_30_pp and Ir_30_pp_150R (PDF)

■ AUTHOR INFORMATION

Corresponding Author

Herbert Over − *Institute of Physical Chemistry, Justus Liebig University, Giessen D-35392, Germany; Center for Materials Research, Justus Liebig University, Giessen D-35392, Germany;* orcid.org/0000-0001-7689-7385; Email: Herbert.Over@phys.chemie.uni-giessen.de

Authors

Wei Wang − *Institute of Physical Chemistry, Justus Liebig University, Giessen D-35392, Germany; Center for Materials Research, Justus Liebig University, Giessen D-35392, Germany*

Matej Zlatar − *Helmholtz Institute Erlangen-Nürnberg for Renewable Energy (IEK-11), Forschungszentrum Jülich GmbH, Erlangen D-91058, Germany; Department of Chemical and Biological Engineering, Friedrich-Alexander-Universität Erlangen-Nürnberg, Erlangen D-91058, Germany;* orcid.org/0000-0003-1041-5149

Yu Wang − *Institute of Physical Chemistry, Justus Liebig University, Giessen D-35392, Germany; Center for Materials Research, Justus Liebig University, Giessen D-35392, Germany*

Phillip Timmer − *Institute of Physical Chemistry, Justus Liebig University, Giessen D-35392, Germany; Center for Materials Research, Justus Liebig University, Giessen D-35392, Germany*

Alexander Spriewald-Luciano − *Institute of Physical Chemistry, Justus Liebig University, Giessen D-35392, Germany; Center for Materials Research, Justus Liebig University, Giessen D-35392, Germany;* orcid.org/0000-0002-6375-4809

Lorena Glatthaar − *Institute of Physical Chemistry, Justus Liebig University, Giessen D-35392, Germany; Center for Materials Research, Justus Liebig University, Giessen D-35392, Germany*

Serhiy Cherevko − *Helmholtz Institute Erlangen-Nürnberg for Renewable Energy (IEK-11), Forschungszentrum Jülich GmbH, Erlangen D-91058, Germany;* orcid.org/0000-0002-7188-4857

Complete contact information is available at: https://pubs.acs.org/10.1021/acscatal.5c00588

Notes

The authors declare no competing financial interest.

■ ACKNOWLEDGMENTS

L.G. and H.O. acknowledge funding by the Deutsche Forschungsgemeinschaft (DFG, SPP2080, German Research Foundation 493681475).

https://doi.org/10.1021/acscatal.5c00588
ACS Catal. 2025, 15, 6721−6730

REFERENCES

(1) Argyrou, M. C.; Christodoulides, P.; Kalogirou, S. A. Energy Storage for Electricity Generation and Related Processes: Technologies Appraisal and Grid Scale Applications. *Renew. Sustain. Energy Rev.* **2018**, *94*, 804−821.

(2) Chatenet, M.; Pollet, B. G.; Dekel, D. R.; Dionigi, F.; Deseure, J.; Millet, P.; Braatz, R. D.; Bazant, M. Z.; Eikerling, M.; Staffell, I.; Balcombe, P.; Shao-Horn, Y.; Schäfer, H. Water Electrolysis: from Textbook Knowledge to the Latest Scientific Strategies and Industrial Developments. *Chem. Soc. Rev.* **2022**, *51*, 4583−4762.

(3) Crabtree, G. W.; Dresselhaus, M. S.; Buchanan, M. V. The Hydrogen Economy. *Phys. Today* **2004**, *57*, 39−44.

(4) Carmo, M.; Fritz, D. L.; Mergel, J.; Stolten, D. A Comprehensive Review on PEM Water Electrolysis. *Int. J. Hydrog. Energy* **2013**, *38*, 4901−4934.

(5) Zeradjanin, A. R.; Masa, J.; Spanos, I.; Schlögl, R. Oxygen Evolution Reaction − From Mechanistic Controveries Toward Relevant Electrocatalytic Descriptors. *Front. Energy Res.* **2021**, *8*, No. 613092.

(6) Galyamin, D.; Tolosana-Moranchel, Á.; Retuerto, M.; Rojas, S. Unraveling the Most Relevant Features for the Design of Iridium Mixued Oxides with High Activity and Durability for the Oxygen Evolution Reaction in Acidic Media. *JACS Au* **2023**, *3*, 2336−2355.

(7) Sharma, S. K.; Wu, C.; Malone, N.; Titheridge, L. J.; Zhao, C.; Gupta, P.; Idriss, H.; Kennedy, J. V.; Jovic, V.; Marshall, A. T. Ru-Based Catalysts for Proton Exchange Membrane Water Electrolysis: The Need to Look Beyond Another Catalyst. *Int. J. Hydrog. Energy* **2025**, *102*, 1461−1479.

(8) Bernsmeier, D.; Bernicke, M.; Schmack, R.; Sachse, B.; Paul, R.; Bergmann, A.; Strasser, P.; Ortel, E.; Kraehnert, R. Oxygen Evolution Catalysts Based on Ir-Ti Mixed Oxides with Templated Mesopore Structure: Impact of Ir on Activity and Conductivity. *ChemSusChem* **2018**, *11*, 2367−2374.

(9) Frisch, M.; Raza, M. H.; Ye, M.; Sachse, R.; Paul, B.; Gunder, R.; Pinna, N.; Kraehnert, R. ALD-Coated Mesoporous Iridium-Titanium Mixed Oxides: Maximizing Iridium Utilization for an Outstanding OER Performance. *Adv. Mater. Interfaces* **2022**, *9*, No. 2102035.

(10) Trasatti, S. Electrocatalysis: Understanding the Success of DSA®. *Electrochim. Acta* **2000**, *45*, 2377−2385.

(11) van der Merwe, M.; Garcia-Diez, R.; Lahn, L.; Wibowo, R. E.; Frisch, J.; Gorgoi, M.; Yang, W.; Ueda, S.; Wilks, R. G.; Kasian, O.; Bär, M. The Chemical and Electronic Properties of Stability-Enhanced, Mixed Ir-TiO_x Oxygen Evolution Reaction Catalysts. *ACS Catal.* **2023**, *13*, 15427−15438.

(12) Ortel, E.; Reier, T.; Strasser, P.; Kraehnert, R. Mesoporous IrO_2 Films Templated by PEO-PB-PEO Block-Copolymers: Self-Assembly, Crystallization Behavior, and Electrocatalytic Performance. *Chem. Mater.* **2011**, *23*, 3201−3209.

(13) Nong, H. N.; Gan, L.; Willinger, E.; Teschner, D.; Strasser, P. IrO_x Core-Shell Nanocatalysts for Cost- and Energy-Efficient Electrochemical Water Splitting. *Chem. Sci.* **2014**, *5*, 2955−2963.

(14) Dang, Q.; Lin, H.; Fan, Z.; Ma, L.; Shao, Q.; Ji, Y.; Zheng, F.; Geng, S.; Yang, S. Z.; Kong, N.; Zhu, W.; Li, Y.; Liao, F.; Huang, X.; Shao, M. Iridium Metallene Oxide for Acidic Oxygen Evolution Catalysis. *Nat. Commun.* **2021**, *12*, 6007.

(15) Song, J.; Wei, C.; Huang, Z.-F.; Liu, C.; Zeng, L.; Wang, X.; Xu, Z. J. A Review on Fundamentals for Designing Oxygen Evolution Electrocatalysts. *Chem. Soc. Rev.* **2020**, *49*, 2196−2214.

(16) Kasian, O.; Grote, J.-P.; Geiger, S.; Cherevko, S.; Mayrhofer, K. J. J. The Common Intermediates of Oxygen Evolution and Dissolution Reactions during Water Electrolysis on Iridium. *Angew. Chem., Int. Ed.* **2018**, *57*, 2488−2491.

(17) Lončar, A.; Escalera-López, D.; Cherevko, S.; Hodnik, N. Inter-relationships between Oxygen Evolution and Iridium Dissolution Mechanisms. *Angew. Chem., Int. Ed.* **2022**, *61*, No. e202114437.

(18) Seitz, L. C.; Dickens, C. F.; Nishio, K.; Hikita, Y.; Montoya, J.; Doyle, A.; Kirk, C.; Vojvodic, A.; Hwang, H. Y.; Norskov, J. K.; Jaramillo, T. F. A Highly Active and Stable $IrO_x/SrIrO_3$ Catalyst for the Oxygen Evolution Reaction. *Science* **2016**, *353*, 1011−1014.

(19) Lee, S.; Lee, Y. J.; Lee, G.; Soon, A. Activated Chemical Bonds in Nanoporous and Amorphous Iridium Oxides Favor Low Overpotential for Oxygen Evolution Reaction. *Nat. Commun.* **2022**, *13*, 3171.

(20) Velasco Vélez, J. J.; Bernsmeier, D.; Mom, R. V.; Zeller, P.; Shao-Horn, Y.; Roldan Cuenya, B.; Knop-Gericke, A.; Schlögl, R.; Jones, T. E. Iridium Oxide Coordinatively Unsaturated Active Sites Govern the Electrocatalytic Oxidation of Water. *Adv. Energy Mater.* **2024**, *14*, No. 2303407.

(21) Gao, J.; Xu, C.-Q.; Hung, S.-F.; Liu, W.; Cai, W.; Zeng, Z.; Jia, C.; Chen, H. M.; Xiao, H.; Li, J.; Huang, Y.; Liu, B. Breaking Long-range Order in Iridium Oxide by Alkali Ion for Efficient Water Oxidation. *J. Am. Chem. Soc.* **2019**, *141*, 3014−3023.

(22) Xu, J.; Jin, H.; Lu, T.; Li, J.; Liu, Y.; Davey, K.; Zheng, Y.; Qiao, S. Z. $IrO_x{\cdot}nH_2O$ with Lattice Water-Assisted Oxygen Exchange for High-Performance Proton Exchange Membrane Water Electrolyzers. *Sci. Adv.* **2023**, *9*, No. eadh1718.

(23) Reier, T.; Pawolek, Z.; Cherevko, S.; Bruns, M.; Jones, T.; Teschner, D.; Selve, S.; Bergmann, A.; Nong, H. N.; Schlögl, R.; Mayrhofer, K. J. J.; Strasser, P. Molecular Insight in Structure and Activity of Highly Efficient, Low-Ir Ir-Ni Oxide Catalysts for Electrochemical Water Splitting (OER). *J. Am. Chem. Soc.* **2015**, *137*, 13031−13040.

(24) Thao, N. T. T.; Jang, J. U.; Nayak, A. K.; Han, H. Current Trends of Iridium-Based Catalysts for Oxygen Evolution Reaction in Acidic Water Electrolysis. *Small Sci.* **2024**, *4*, No. 2300109.

(25) Spöri, C.; Briois, P.; Nong, H. N.; Reier, T.; Billard, A.; Kühl, S.; Teschner, D.; Strasser, P. Experimental Activity Descriptors for Iridium-Based Catalysts for the Electrochemical Oxygen Evolution Reaction (OER). *ACS Catal.* **2019**, *9*, 6653−6663.

(26) Escalera-López, D.; Czioska, S.; Geppert, J.; Boubnov, A.; Röse, P.; Saraçi, E.; Krewer, U.; Grunwaldt, J. D.; Cherevko, S. Phase- and Surface Composition-Dependent Electrochemical Stability of Ir-Ru Nanoparticles during Oxygen Evolution Reaction. *ACS Catal.* **2021**, *11*, 9300−9316.

(27) Park, Y.; Jang, H. Y.; Lee, T. K.; Kim, T.; Kim, D.; Kim, D.; Baik, H.; Choi, J.; Kwon, T.; Yoo, S. J.; Back, S.; Lee, K. Atomic-Level Ru-Ir Mixing in Rutile-Type $(RuIr)O_2$ for Efficient and Durable Oxygen Evolution Catalysis. *Nat. Commun.* **2025**, *16*, 579.

(28) Wang, W.; Timmer, P.; Luciano, A. S.; Wang, Y.; Weber, T.; Glatthaar, L.; Guo, Y.; Smarsly, B. M.; Over, H. Inserted Hydrogen Promotes Oxidation Catalysis of Mixed $Ru_{0.3}Ti_{0.7}O_2$ as Exemplified with Total Propane Oxidation and the HCl Oxidation Reaction. *Catal. Sci. Technol.* **2023**, *13*, 1395−1408.

(29) Hao, H.; Liu, Z.; Zhao, F.; Li, W. Natural Gas as Vehicle Fuel in China: A Review. *Renew. Sustain. Energy Rev.* **2016**, *62*, 521−533.

(30) Reichert, D.; Stöwe, K. Sol-Gel-Syntheses and Structural as well as Electrical Characterizations of Anatase- and Rutile-type Solid Solutions in the System IrO_2-TiO_2. *ChemistryOpen* **2023**, *12*, No. e202300032.

(31) Khalid, O.; Weber, T.; Drazic, G.; Djerdj, I.; Over, H. Mixed $Ru_xIr_{1-x}O_2$ Oxide Catalyst with Well-Defined and Varying Composition Applied to CO Oxidation. *J. Phys. Chem. C* **2020**, *124*, 18670−18683.

(32) Klemm, S. O.; Topalov, A. A.; Laska, C. A.; Mayrhofer, K. J. J. Coupling of a High Throughput Microelectrochemical Cell with Online Multielemental Trace Analysis by ICP-MS. *Electrochem. Commun.* **2011**, *13*, 1533−1535.

(33) Cherevko, S.; Geiger, S.; Kasian, O.; Kulyk, N.; Grote, J.-P.; Savan, A.; Shrestha, B. R.; Merzlikin, S.; Breitbach, B.; Ludwig, A.; Mayrhofer, K. J. J. Oxygen and Hydrogen Evolution Reactions on Ru, RuO_2, Ir, and IrO_2 Thin Film Electrode in Acidic and Alkaline Electrolytes: A Comparative Study on Activity and Stability. *Catal. Today* **2016**, *262*, 170−180.

(34) Zlatar, M.; Escalera-López, D.; Rodríguez, M. G.; Hrbek, T.; Götz, C.; Mary Joy, R.; Savan, A.; Tran, H. P.; Nong, H. N.; Pobedinskas, P.; Briega-Martos, V.; Hutzler, A.; Böhm, T.; Haenen, K.; Ludwig, A.; Khalakhan, I.; Strasser, P.; Cherevko, S. Standardizing OER Electrocatalyst Benchmarking in Aqueous Electrolytes:

https://doi.org/10.1021/acscatal.5c00588
ACS Catal. 2025, 15, 6721−6730

Comprehensive Guidelines for Accelerated Stress Tests and Backing Electrodes. *ACS Catal.* **2023**, *13*, 15375−15392.
(35) Shang, H.; Li, M.; Li, H.; Huang, C.; Mao, C.; Ai, Z.; Zhang, L. Oxygen Vacancies Promoted the Selective Photocatalytic Removal of NO with Blue TiO_2 via Simultaneous Molecular Oxygen Activation and Photogenerated Hole Annihilation. *Environ. Sci. Technol.* **2019**, *53*, 6444−6453.
(36) Liu, H.; Ma, H. T.; Li, X. Z.; Li, W. Z.; Wu, M.; Bao, X. H. The enhancement of TiO_2 photocatalytic activity by hydrogen thermal treatment. *Chemosphere* **2003**, *50*, 39−46.
(37) Chen, H.; Gao, P.; Liu, Z.; Liang, L.; Han, Q.; Wang, Z.; Chen, K.; Zhao, Z.; Guo, M.; Liu, X.; Han, X.; Bao, X.; Hou, G. Direct Detection of Reactive Gallium-Hydride Species on the Ga_2O_3 Surface via Solid-State NMR Spectroscopy. *J. Am. Chem. Soc.* **2022**, *144*, 17365−17375.
(38) Freakley, S. J.; Ruiz-Esquius, J.; Morgan, D. J. The X-ray Photoelectron Spectra of Ir, IrO_2 and $IrCl_3$ revisited. *Surf. Interface Anal.* **2017**, *49*, 794−799.
(39) Pfeifer, V.; Jones, T. E.; Velasco Vélez, J. J.; Massué, C.; Arrigo, R.; Teschner, D.; Girgsdies, F.; Scherzer, M.; Greiner, M. T.; Allan, J.; Hashagen, M.; Weinberg, G.; Piccinin, S.; Hävecker, M.; Knop-Gericke, A.; Schlögl, R. The Electronic Structure of Iridium and its Oxides. *Surf. Int. Anal.* **2016**, *48*, 261−273.
(40) Kahk, J. M.; Poll, C. G.; Oropeza, F. E.; Ablett, J. M.; Céolin, D.; Rueff, J.-P.; Agrestini, S.; Utsumi, Y.; Tsuei, K. D.; Liao, Y. F.; Borgatti, F.; Panaccione, G.; Regoutz, A.; Egdell, R. G.; Morgan, B. J.; Scanlon, D. O.; Payne, D. J. Understanding the Electronic Structure of IrO_2 Using Hard-X-ray Photoelectron Spectroscopy and Density-Functional Theory. *Phys. Rev. Lett.* **2014**, *112*, No. 117601.
(41) Exner, K. S.; Sohrabnejad-Eskan, I.; Over, H. A Universal Approach to Determine the Free Energy Diagram of an Electrocatalytic Reaction. *ACS Catal.* **2018**, *8*, 1864−1879.
(42) Fang, Y. H.; Liu, Z. P. Tafel Kinetics of Electrocatalytic Reactions: From Experiment to First Principles. *ACS Catal.* **2014**, *4*, 4364−4376.
(43) Exner, K. S.; Over, H. Beyond the Rate-Determining Step in the Oxygen Evolution Reaction over a Single-Crystalline IrO_2(110) Model Electrode: Kinetic Scaling. *ACS Catal.* **2019**, *9*, 6755−6765.
(44) Kuo, D. Y.; Kawasaki, J. K.; Nelson, J. N.; Kloppenburg, J.; Hautier, G.; Shen, K. M.; Schlom, D. G.; Suntivich, J. Influence of Surface Adsorption on the Oxygen Evolution Reaction on IrO_2(110). *J. Am. Chem. Soc.* **2017**, *139*, 3473−3479.
(45) Nong, H. N.; Falling, L. J.; Bergmann, A.; Klingenhof, M.; Tran, H. P.; Spöri, C.; Mom, R.; Timoshenko, J.; Zichittella, G.; Knop-Gericke, A.; Piccinin, S.; Pérez-Ramírez, J.; Cuenya, B. R.; Schlögl, R.; Strasser, P.; Teschner, D.; Jones, T. E. Key Role of Chemistry Versus Bias in Electrocatalytic Oxygen Evolution. *Nature* **2020**, *587*, 408−414.
(46) Danilovic, N.; Subbaraman, R.; Chang, K.-C.; Chang, S. H.; Kang, Y. J.; Snyder, J.; Paulikas, A. P.; Strmcnik, D.; Kim, Y.-T.; Myers, D.; Stamenkovic, V. R.; Markovic, N. M. Activity-Stability Trends for the Oxygen Evolution Reaction on Monometallic Oxides in Acidic Environments. *J. Phys. Chem. Lett.* **2014**, *5*, 2474−2478.
(47) Zlatar, M.; Nater, D.; Escalera-López, D.; Joy, R. M.; Pobedinskas, P.; Haenen, K.; Copéret, C.; Cherevko, S. Evaluating the Stability of Ir Single Atom and Ru Atomic Cluster Oxygen Evolution Reaction Electrocatalysts. *Electrochim. Act.* **2023**, *444*, No. 141982.
(48) Wang, W.; Wang, Y.; Timmer, P.; Spriewald-Luciano, A.; Weber, T.; Glatthaar, L.; Guo, Y.; Smarsly, B. M.; Over, H. Hydrogen Incorporation in $Ru_xTi_{1-x}O_2$ Mixed Oxides Promotes Total Oxidation of Propane. *Inorganics* **2023**, *11*, 330.
(49) Mavrikakis, M.; Hammer, B.; Nørskov, J. K. Effect of Strain on the Reactivity of Metal Surfaces. *Phys. Rev. Lett.* **1998**, *81*, 2819−2822.
(50) Hammer, B.; Nørskov, J. K. Electronic Factors Determining the Reactivity of Metal Surfaces. *Surf. Sci.* **1995**, *343*, 211−220.
(51) Kitchin, J. R.; Nørskov, J. K.; Barteau, M. A.; Chen, J. G. Role of Strain and Ligand Effects in the Modification of the Electronic and Chemical Properties of Bimetallic Surfaces. *Phys. Rev. Lett.* **2004**, *93*, No. 156801.
(52) Strasser, P.; Koh, S.; Anniyev, T.; Greeley, J.; More, K.; Yu, C.; Liu, Z.; Kaya, S.; Nordlund, D.; Ogasawara, H.; Toney, M. F.; Nilsson, A. Lattice-strain Control of the Activity in Dealloyed Core-shell Fuel Cell Catalysts. *Nat. Chem.* **2010**, *2*, 454−460.
(53) Xia, Z.; Guo, S. Strain Engineering of Metal-based Nanomaterials for Energy Electrocatalysis. *Chem. Soc. Rev.* **2019**, *48*, 3265−3278.
(54) You, B.; Tang, M. T.; Tsai, C.; Abild-Pedersen, F.; Zheng, X.; Li, H. Enhancing Electrocatalytic Water Splitting by Strain Engineering. *Adv. Mater.* **2019**, *31*, No. 1807001.
(55) Feng, Z.; Lu, F.; Hu, Q.; Qiu, J.; Lei, X.; Wang, B.; Guo, R.; Tian, Y.; Liu, X.; You, J. Built-in Electric Fields and Extra Electric Fields in the Oxygen Evolution Reaction. *J. Mater. Chem. A* **2024**, *12*, 18047−18070.
(56) Buvat, G.; Eslamibidgoli, M. J.; Youssef, A. H.; Garbarino, S.; Ruediger, A.; Eikerling, M.; Guay, D. Effect of IrO_6 Octahedron Distortion on the OER Activity at (100) IrO_2 Thin Film. *ACS Catal.* **2020**, *10*, 806−817.
(57) Chaudhary, P.; Zagalskaya, A.; Over, H.; Alexandrov, V. Strain-Dependent Activity-Stability Relations in RuO_2 and IrO_2 Oxygen Evolution Catalysts. *ChemElectroChem.* **2024**, *11*, No. e202300659.
(58) Wu, Z.; Cheng, Y.; Tao, F.; Daemen, L.; Foo, G. S.; Nguyen, L.; Zhang, X.; Beste, A.; Ramirez-Cuesta, A. J. Direct Neutron Spectroscopy Observation of Cerium Hydride Species on a Cerium Oxide Catalyst. *J. Am. Chem. Soc.* **2017**, *139*, 9721−9727.
(59) Li, Z.; Werner, K.; Qian, K.; You, R.; Płucienik, A.; Jia, A.; Wu, L.; Zhang, L.; Pan, H.; Kuhlenbeck, H.; Shaikhutdinov, S.; Huang, W.; Freund, H.-J. Oxidation of Reduced Ceria by Incorporation of Hydrogen. *Angew. Chem., Int. Ed.* **2019**, *58*, 14686−14693.
(60) Vilé, G.; Bridier, B.; Wichert, J.; Pérez-Ramírez, J. Ceria in Hydrogenation Catalysis: High Selectivity in the Conversion of Alkynes to Olefins. *Angew. Chem., Int. Ed.* **2012**, *51*, 8620−8623.
(61) Carrasco, J.; Vilé, G.; Fernández-Torre, D.; Pérez, R.; Pérez-Ramírez, J.; Ganduglia-Pirovano, M. V. Molecular-Level Understanding of CeO_2 as a Catalyst for Partial Alkyne Hydrogenation. *J. Phys. Chem. C* **2014**, *118*, 5352−5360.
(62) Bavykin, D. V.; Carravetta, M.; Kulak, A. N.; Walsh, F. C. Application of Magic-Angle Spinning NMR to Examine the Nature of Protons in Titanate Nanotubes. *Chem. Mater.* **2010**, *22*, 2458−2465.
(63) Jiang, Y.; Huang, J.; Dai, W.; Hunger, M. Solid-State Nuclear Magnetic Resonance Investigations of the Nature, Property, and Activity of Acid Sites on Solid Catalysts. *Solid State Nucl. Magn. Reson.* **2011**, *39*, 116−141.
(64) Guo, Y.; Chen, S.; Yu, Y.; Tian, H.; Zhao, Y.; Ren, J. C.; Huang, C.; Bian, H.; Huang, M.; An, L.; Li, Y.; Zhang, R. Hydrogen-Location-Sensitive Modulation of the Redox Reactivity for Oxygen-Deficient TiO_2. *J. Am. Chem. Soc.* **2019**, *141*, 8407−8411.
(65) Xie, L.; Zhu, Q.; Zhang, G.; Ye, K.; Zou, C.; Prezhdo, O. V.; Wang, Z.; Luo, Y.; Jiang, J. Tunable Hydrogen Doping of Metal Oxide Semiconductors with Acid-Metal Treatment at Ambient Conditions. *J. Am. Chem. Soc.* **2020**, *142*, 4136−4140.
(66) Hu, Z.; Wang, Z.; Guo, Y.; Wang, L.; Guo, Y. L.; Zhang, J. S.; Zhan, W. C. Total oxidation of Propane over a Ru/CeO_2 Catalyst at Low Temperature. *Environ. Sci. Technol.* **2018**, *52*, 9531−9541.
(67) Freyschlag, C. G.; Madix, R. J. Precious Metal Magic: Catalytic Wizardy. *Mater. Tod.* **2011**, *14*, 134−142.
(68) Ma, L.; Geng, Y.; Chen, X. Y.; Yan, N. Q.; Li, J. H.; Schwank, J. W. Reaction mechanism of propane oxidation over Co_3O_4 nanorods as rivals of platinum catalysts. *Chem. Eng. J.* **2020**, *402*, No. 125911.
(69) Man, I. C.; Su, H.; Calle-Vallejo, F.; Hansen, H. A.; Martínez, J. I.; Inoglu, N. G.; Kitchin, J.; Jaramillo, T. F.; Nørskov, J. K.; Rossmeisl, J. Universality in Oxygen Evolution Electrocatalysis on Oxide Surface. *ChemCatChem.* **2011**, *3*, 1159−1165.
(70) Exner, K. S. Four Generations of Volcano Plots for the Oxygen Evolution Reaction: Beyond Proton-Coupled Electron Transfer Steps? *Acc. Chem. Res.* **2024**, *57*, 1336−1345.

https://doi.org/10.1021/acscatal.5c00588
ACS Catal. 2025, 15, 6721−6730

(71) Du, M.; Yu, F.; Gong, S.; Liu, F. Design of Electrocatalysts with High Performance Based on Thermodynamics and Kinetics: Progress and Prospects. *Adv. Funct. Mater.* **2025**, *35*, No. 2413826.
(72) Carbonio, E. A.; Sulzmann, F.; Teschner, D.; Velasco-Vélez, J. J.; Hävecker, M.; Gericke, A. K.; Schlögl, R.; Jones, T. Thermal Synthesis of Electron Deficient Oxygen Species on Crystalline IrO_2. *Catal. Sci. Technol.* **2024**, *14*, 572−580.
(73) Chen, S.-H.; Yang, Y.-F.; Song, Z.-Y.; Xiao, X.-Y.; Huang, C.-C.; Cai, X.; Li, P.-H.; Yang, M.; Chen, A.; Liu, W.-Q.; Huang, X.-J. Modulating Paired Ir−O−Ir via Electronic Perturbations of Correlated Ir Single Atoms to Overcome Catalytic Selectivity. *Chem. Sci.* **2023**, *14*, 9678−9688.
(74) Velasco Vélez, J. J.; Bernsmeier, D.; Mom, R. V.; Zeller, P.; Shao-Horn, Y.; Roldan Cuenya, B.; Knop-Gericke, A.; Schlögl, R.; Jones, T. E. Iridium Oxide Coordinatively Unsaturated Active Sites Govern the Electrocatalytic Oxidation of Water. *Adv. Energy Mater.* **2024**, No. 2303407.

https://doi.org/10.1021/acscatal.5c00588
ACS Catal. 2025, 15, 6721−6730